



# Synthesis, physical and semiconducting properties of SnS<sub>2</sub> prepared by chemical route

S. Kabouche<sup>1</sup> · Y. Louafi<sup>1</sup> · J.-F. Bardeau<sup>2</sup> · M. Trari<sup>3</sup>

Received: 12 August 2018 / Accepted: 2 November 2018 / Published online: 11 November 2018  
© Springer Science+Business Media, LLC, part of Springer Nature 2018

## Abstract

The present study focused on the physical and electrochemical properties of stannic sulfide SnS<sub>2</sub> synthesized by a template-free chemical route using thiourea as a precursor. SnS<sub>2</sub> powder was characterized by X-ray diffraction (XRD), diffuse reflectance and Raman. The XRD pattern confirmed the formation of the hexagonal phase SnS<sub>2</sub> (SG: *P-3m1*) with the lattice parameters  $a = 3.639 \text{ \AA}$ ,  $c = 5.868 \text{ \AA}$  and a mean crystallite size of  $\sim 60 \text{ nm}$ . The optical measurements gave a direct transition of 2.26 eV, further transition indirectly allowed was observed at 1.63 eV. The Mott-Schottky plot recorded in Na<sub>2</sub>SO<sub>4</sub> (0.1 M) electrolyte exhibits a linear behavior, characteristic of *n*-type conductivity and confirmed by chronoamperometry. The flat band potential ( $-0.63 \text{ V}_{\text{SCE}}$ ) is close to the photocurrent onset potential ( $E_{\text{on}} = -0.64 \text{ V}_{\text{SCE}}$ ) and a donor density of  $3.54 \times 10^{16} \text{ cm}^{-3}$  was determined. The electrochemical impedance spectroscopy measured in the range ( $10^{-2} - 5 \times 10^4 \text{ Hz}$ ) showed two semicircles assigned to a faradic charge transfer ( $R_{\text{ct}} = 2.46 \text{ k}\Omega \text{ cm}^2$ ) and grain boundaries contribution ( $R_{\text{gb}} = 13.69 \text{ k}\Omega \text{ cm}^2$ ). The conduction band, located at  $-4.02 \text{ eV}$  below vacuum, is made up of Sn<sup>4+</sup>:  $5p$  while the valence band ( $-6.28 \text{ eV}$ ) derives mainly from S<sup>2-</sup>:  $3p$ . As an application, Rhodamine B was successfully oxidized by photocatalysis on SnS<sub>2</sub>, 93.67% of the initial concentration ( $10 \text{ mg L}^{-1}$ ) disappeared after 3 h of exposure to solar light ( $90 \text{ mW cm}^{-2}$ ).

## 1 Introduction

The chalcogenide compounds were not well-studied compared to oxides but begin to attract a growing interest in solar devices and photoelectrochemical (PEC) cells [1]. The binary system Sn–S shows a variety of phases Sn<sub>*x*</sub>S<sub>*y*</sub>, due to the versatile coordination of both tin and sulfur [2]. Researchers are paying a great attention toward SnS<sub>2</sub> compound for its many applications in the visible-light-driven photocatalysis [3], biosensors, anode materials for Li-ion batteries [4], solar cell [5], photochemical hydrogen generation and photodegradation of organic pollutants [6]. The

berndtite (SnS<sub>2</sub>) is reported to be the *n*-type semiconductor with a hexagonal crystalline structure and a band gap in the range (2.18–2.44 eV), depending on the synthesis method [7]. It possesses interesting properties, abundant in the earth, low-cost, good chemical and thermal stabilities and is environmental-friendly [8]. The compound is formed by Sn atoms sandwiched between two S layers with strong Sn–S bonds and weak Van der Waals interlayer interactions [9]. The control of the shape and size of nanostructures has been investigated in recent years [10–13]. Up to now, SnS<sub>2</sub> was produced with different morphologies by hydrothermal route [14], thermal sulfurization [15], dip coating, chemical spray pyrolysis [16] chemical vapor deposition [17], solvothermal process, reflux synthesis [18], microwave-assistant method [19] and SILAR technique [20]. Therefore, because of these preparations, SnS<sub>2</sub> displays various morphologies, such as nanotubes, nanorods [21], nanoflowers, nanoflakes [22], nanosheets, thin films [23], nanoplate [24], nanoparticles and nanobelt [25]. Accordingly, simple methods need to be developed to overcome the complexity and the high cost of these techniques.

In this paper, we describe a simple chemical method to synthesize SnS<sub>2</sub>, the physical parameters such as the reaction time, temperature and concentration of organic ligands can

✉ M. Trari  
solarchemistry@gmail.com; mtrari@usthb.dz

<sup>1</sup> Laboratory of Electrochemistry-Corrosion, Metallurgy and Inorganic Chemistry, Faculty of Chemistry, U.S.T.H.B., BP 32, 16111 Algiers, Algeria

<sup>2</sup> Institut des Molécules et Matériaux du Mans, CNRS n° 6283, Le Mans Université, Avenue Olivier Messiaen, 72085 Le Mans Cedex 9, France

<sup>3</sup> Laboratory of Storage and Valorization of Renewable Energies, Faculty of the Chemistry, U.S.T.H.B., BP 32, 16111 Algiers, Algeria

be easily controlled. Structural properties have been characterized by X-ray diffraction (XRD), diffuse reflectance and Raman spectroscopy. To our knowledge, the photo-electrochemistry and the impedance electrochemical spectroscopy (EIS) have not been reported previously and the energy band diagram as well.

Photocatalysis, as a green chemistry technology, has been attracting remarkable attention in the field of contaminant destruction owing to its very desirable destruction rate as well as its great performance in mineralization [26]. As an application, Rhodamine B (RhB) was degraded upon sunlight by advanced oxidation process (AOP).

## 2 Experimental

SnS<sub>2</sub> powder was prepared by chemical route: appropriate amounts of SnCl<sub>4</sub> (6.5 mL, Fluka Chemie AG, 99.0%) and thiourea (8.42 g, Tu, Fluka AG, 97.0%) were mixed in a round bottom flask containing 50 mL of ethylene glycol (PROLABO). After stirring for 5 min, the reaction mixture was maintained at 160 °C for 1.5 h and naturally cooled to room temperature. A yellow precipitate was collected by decantation since SnS<sub>2</sub> is insoluble in water and dilute acids owing to its low solubility product ( $K_s \sim 10^{-46}$ ). It undergoes successive centrifugations followed by washing with distilled water and acetone to remove chlorides. The precipitate was dried in an air oven at 100 °C and ground in an agate mortar. The X-ray diffraction was done with a Philips X'PERT 1 diffractometer, using filtered Cu-K $\alpha$  radiation ( $\lambda = 0.15418$  nm) and the phase was identified according the PDF-4 database using Highscore Plus. The crystallites size was evaluated from the Williamson-Hall plot using the Xpovder software. The Raman spectrum was recorded in the range (100–1000 cm<sup>-1</sup>) with a confocal microscope Raman spectrometer (JobinYvon, Horiba, T64000), excited by 514 nm line of Ar-Kr ions, with a laser intensity < 1 mW on the sample in order to minimize possible sample deterioration or phase transformation with operating time [27, 28]. The detection system is a high-sensitivity CCD multi-channel detector, cooled to 140 K. The morphology is analyzed with H-4100 FESEM (Hitachi High Technologies Corporation) in Multimode. The optical gap was measured with a Specord 200 plus spectrophotometer; the data were converted to absorbance by using the Kubelka–Munk relation. The physical properties and photoelectrochemical characterizations require compact pellets. SnS<sub>2</sub> (~ 500 mg) was finely ground and pressed into pellets ( $\varnothing = 13$  mm, thickness ~ 2 mm) under 5 kbar. The electrical contact on the pellets was carried out with a wire welded copper and Ag-cement. The assembly was isolated in a glass tube by epoxy resin so that only one side (0.35 cm<sup>2</sup>) was in direct contact with the electrolytic solution. The electrodes were

polished with polishing disks (ECAPOL 2B) and washed thoroughly with distilled water to remove any adhering impurity. The working solution was prepared by dissolving Na<sub>2</sub>SO<sub>4</sub> (0.1 M, Biochem Chemopharma, 99.0%) in distilled water. The electrochemical measurements were performed in a three electrode cell: a saturated calomel electrode (SCE), Pt counter electrode and the working electrode; the temperature was maintained at  $25 \pm 1$  °C using a thermostated bath (Wise Circu). The measurements were plotted with an electrochemical interface (Solartron, SI: 1287) controlled by the Corrview software and a frequency analyzer (Solartron, SI: 1260) driven by the Z-VIEW software, the potential scan was fixed at 10 mV s<sup>-1</sup>. A tungsten lamp (200 W) was used for the photoelectrochemical study.

The photocatalytic experiments were carried out in an open Pyrex batch reactor (100 mL) exposed to solar light; the flux (80 mW cm<sup>-2</sup>), measured with a light meter (Testo 545) at the reactor surface. The tests were performed with a volume of 50 mL of RhB solution (10 mg L<sup>-1</sup>) in presence of SnS<sub>2</sub> (50 mg) under continuous stirring. The reactor is cooled by water circulation. Before irradiation, the suspensions were kept overnight in the dark to reach equilibrium, then 2 mL was taken for analysis (adsorption). Under irradiation, the samples were centrifuged and filtered using micros filters (0.45  $\mu$ m) and analyzed by UV-Visible spectrophotometry (Specord 200plus).

## 3 Results and discussion

From the XRD pattern (Fig. 1a), the crystal structure of the synthesized SnS<sub>2</sub> powder was identified as the Berndtite phase in agreement with the PDF-4 database (No. 00-001-1010). All peaks are indexed in the hexagonal system (space group: *P-3m1*), with lattice parameters  $a = 3.639$  Å and  $c = 5.868$  Å. The high intensity and narrow peaks indicate a good crystallinity. The crystallite size (*D*) of SnS<sub>2</sub> is evaluated from the Williamson–Hall plot (Fig. 1b) by extrapolation to  $\theta = 0$ , the *D* value (59 nm) indicates nanocrystallites. Assuming spherical particles with non-porous nature, a minimal active surface area ( $S_s$ ) of 21 m<sup>2</sup> g<sup>-1</sup> = (6/ $\rho D$ ) is obtained.  $\rho$  is the experimental density (= 4.86 g cm<sup>-3</sup>).

The Raman spectroscopy was undertaken to investigate the chemical structure and vibration properties of SnS<sub>2</sub>. The spectrum (Fig. 2) shows a sharp and intense peak at 317 cm<sup>-1</sup>, attributed to the active vibration mode A<sub>1g</sub> (Sn–S) of the hexagonal phase SnS<sub>2</sub> [29, 30]; such characterization confirms the existence of simple phase SnS<sub>2</sub>. “A” means a non-degenerate mode while the subscript “g” indicates the parity under inversion of the centro-symmetric space group. The morphology of the sample was observed by scanning electron microscopy (SEM) (Fig. 3). SnS<sub>2</sub> shows 3D microspheres with a diameter of 2–3  $\mu$ m.

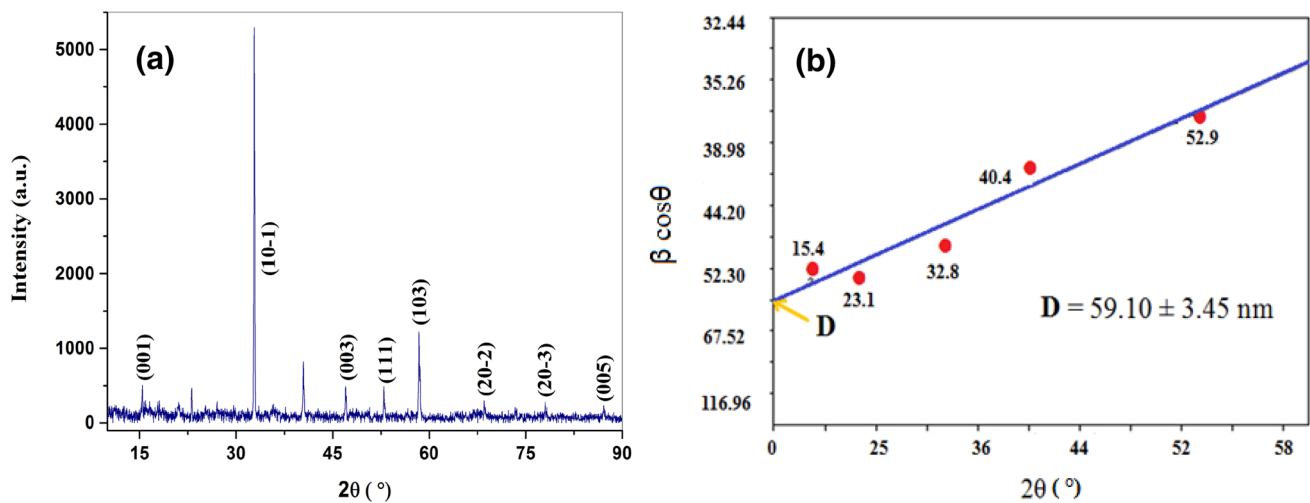


**Fig. 1** **a** XRD pattern of SnS<sub>2</sub> prepared by chemical route. **b** The crystallite size determined from the Williamson–Hall plot

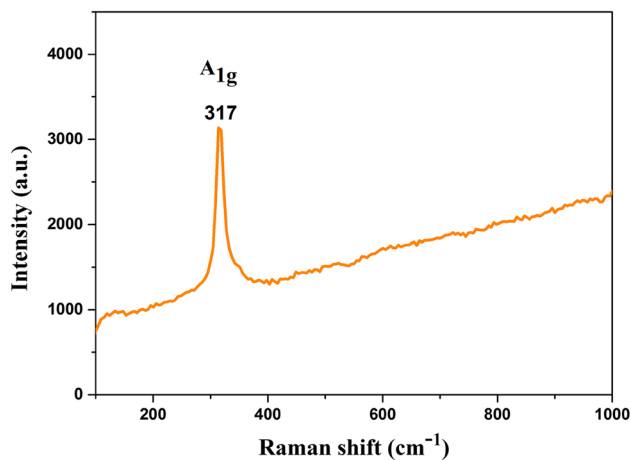


**Fig. 2** Raman spectrum of SnS<sub>2</sub>

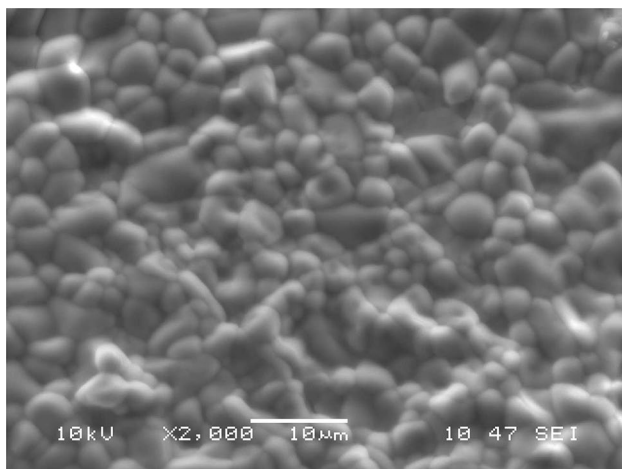


**Fig. 3** SEM Images of the bulk SnS<sub>2</sub>

SnS<sub>2</sub> is a potential candidate in photocatalysis and the optical band gap ( $E_g$ ) is crucial for the solar energy conversion; its value is evaluated from the Tauc relation [31]:

$$(\alpha h\nu)^k = B(h\nu - E_g) \quad (1)$$

where  $h\nu$  is the photon energy,  $B$  a proportionality constant and the exponent  $k$  is equal to 2 or 1/2 for direct or indirect transition respectively. The gap  $E_g$  ( $=2.26$  eV) is deduced from the intersection of the extrapolated line  $(\alpha h\nu)^k$  with the  $h\nu$ -axis and the transition are directly allowed ( $k=2$ ) in agreement with that reported elsewhere [7]. However, the energy band gap of the bulk SnS<sub>2</sub> is lower than that observed in thin films. Further indirect transition is observed 1.63 eV (Fig. 4, inset). The absorption coefficient ( $\alpha$ ) is determined by the Kubelka–Munk function [32]:

$$F(R) = \alpha = (1 - R)^2 / 2R \quad (2)$$

where  $R$  is the diffuse reflectance,  $\alpha \sim 2.33$  cm<sup>-1</sup> at 548 nm,  $\alpha^{-1}$  represents the length penetration for a given wavelength.

The electro-kinetic parameters are deduced from the Tafel method (Fig. 5, inset). The exchange current density (0.214 mA cm<sup>-2</sup>) and the corrosion potential ( $-489$  mV) indicate a long lived material.

The flat band potential ( $E_{fb}$ ) is the key parameter in photo-electrochemistry because it gives not only the energy of the valence and conduction bands of the semiconductor but also the conductivity type.  $E_{fb}$  is accurately determined from the capacitance measurement; the technique consists of measuring the reciprocal square capacity ( $C^{-2}$ ) of the semiconductor/electrolyte interface against the potential ( $E$ ):

$$C^{-2}SC = \pm(2/e\epsilon\epsilon_0N_D)(E - E_{fb}) \quad (3)$$

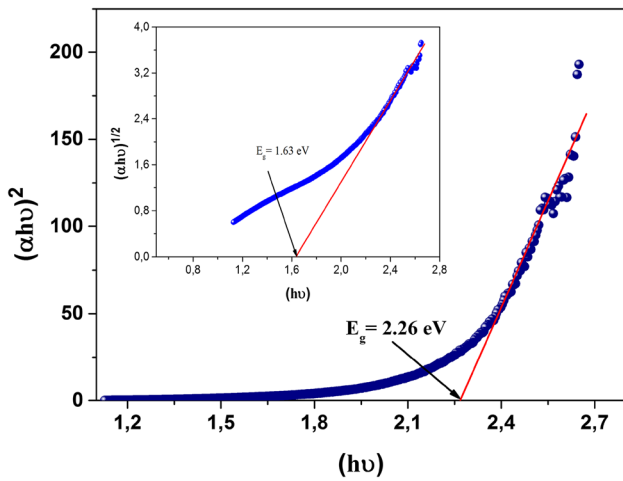


**Fig. 4** Tauc plot  $(\alpha h\nu)^2$  versus.  $h\nu$ . Inset: the indirect transition of  $\text{SnS}_2$

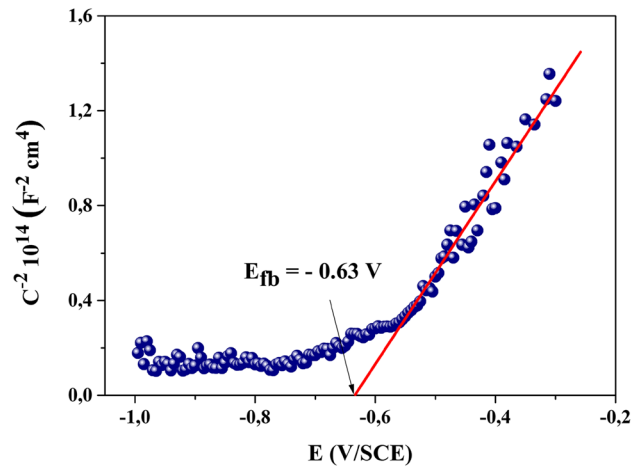


**Fig. 6** Mott–Schottky plot of the junction  $\text{SnS}_2/\text{Na}_2\text{SO}_4$  (0.1 M) measured at 1 KHz

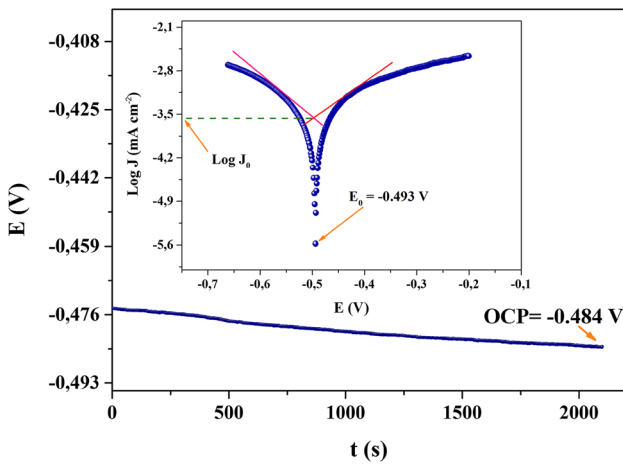


**Fig. 5** Potential plot versus. time of  $\text{SnS}_2$ . Inset: semi-logarithmic plot recorded in  $\text{Na}_2\text{SO}_4$  (0.1 M) electrolyte

where  $e$  is the electron charge,  $\epsilon$  the relative permittivity of  $\text{SnS}_2$  ( $\sim 10.3$ ) [33],  $\epsilon_0$  the permittivity of vacuum ( $8.85 \times 10^{-12} \text{ F m}^{-1}$ ) and  $N_D$  the donor density. The sign  $\pm$  is for  $n$  and  $p$ -types respectively.

The positive slope indicates  $n$ -type conduction (Fig. 6) where the electrons are the majority carriers and their density ( $N_D = 3.54 \times 10^{16} \text{ cm}^{-3}$ ) is deduced from the slope. The extension of the straight line to the abscissa axis gives the potential  $E_{fb}$  ( $-0.63 \text{ V}$ ) which can be assimilated to the Fermi level. The depletion layer ( $W$ ) in which the electro/hole ( $e^-_{CB}, h^+_{VB}$ ) pairs are separated, is calculated from the relation [34]:

$$W = [2\epsilon\epsilon_0(E - E_{fb})/eN_D]^{0.5} \quad (4)$$

The low electron density is in conformity with the medium conductivity of  $\text{SnS}_2$  and produces a wide depletion width ( $W \sim 125 \text{ nm}$ ) calculated for an optimal band bending ( $E - E_{fb}$ ) of  $0.5 \text{ V}$ . Therefore, most ( $e^-_{CB}, h^+_{VB}$ ) pairs generated under illumination are separated by the junction electric field formed spontaneously at the solid/liquid interface.

It is useful to predict theoretically the flat band potentials ( $E_{fb}$ ). A correlation exists between the atomic electronegativities of the constituent atoms and the potential  $E_{fb}$ . However, the flat band potential  $E_{fb}$  and its electron affinity  $E_A$ , can be directly related by the following relation [35]:

$$EA = 4.75 + E_{fb} + \Delta fc + 0.059 \times \Delta pH \quad (5)$$

where  $E_0$  is a constant relating reference electrode to the vacuum level ( $E_0 = 4.75 \text{ eV}$  for SCE),  $\Delta fc$  is the difference between the Fermi level and the bottom of the conduction band for  $n$ -type ( $\Delta fc \sim 0.1 \text{ eV}$ ),  $\Delta pH$  ( $= \text{pH}_{\text{solution}} - \text{pzzp}$ ) is the potential drop across the double layer due to adsorption of  $\text{OH}^-/\text{H}^+$  ions.  $\text{pzzp}$  (1.99) corresponds to  $\text{pH}$  where the net adsorbed charge on the surface is zero and it is the only point where the potential  $E_{fb}$  can be measured, in such a case the electron affinity of  $\text{SnS}_2$  is given by:

$$EA = [\chi^1 S_n \chi^2 S]^{1/3} - 1/2E_g \quad (6)$$

The electron negativity ( $\chi_i$ ) for an atom in the Mulliken scale is the arithmetic mean of the first ionization energy ( $I_1$ ) and the atomic electron affinity ( $A_f$ ):

$$\chi_i = 0.5(I_1 + A_f) \quad (7)$$

The values were taken from the Handbook of Chemistry and Physics [36]. The electronegativity of the

semiconductor is the geometric mean of the electronegativity of the constituent atoms  $\chi$  (6.33 eV); the discrepancy between this value and that predicted from Eq. 6 shows that the latter leads to a useful but rough approximation of electro affinity of the semiconducting compounds. The photocurrent onset potential  $E_{on}$  (−0.77 V), is more negative than that the potential  $E_{fb}$  and this indicates the existence of surface states within the gap region.

The photocurrent ( $J_{ph}$ ) is an intrinsic property of the semiconductor and appears when the electrode is polarized above (resp. below) the potential  $E_{fb}$  for  $n$ -type (resp.  $p$ -type). The current was measured at regular times under chopped visible light. The anodic photocurrent provides a direct confirmation of  $n$ -type conduction properties of  $SnS_2$ . Photons with energy higher than the band gap ( $E_g$ ) are absorbed, producing ( $e^-/h^+$ ) pairs and increases the current density. The average photocurrent was found to be  $65.3 \mu A cm^2$  for a potential of 0.3 V (Fig. 7).

The photocurrent is the difference between the current density under illumination and then in the dark ( $J_D$ ). According to the Gartner model, the photocurrent onset potential ( $E_{on}$ ) is expressed by the relation [37]:

$$(J_{ph} - J_D)^2 = Const \times \alpha^2 W^2 (E - E_{on}) \tag{8}$$

The potential  $E_{on}$  ( $= -0.63$  V) is obtained from the cross point of the line ( $J_{ph}^2 - E$ ) to the potential axis (Fig. 8) and can be reasonable, assimilated to the flat band potential ( $E_{fb}$ ). The positive slope confirms the  $n$ -type behavior (Fig. 8).

The energy of the conduction band (CB) with respect to the vacuum is determined from the combined physical and electrochemical parameters:

$$E_{BC} = -4.75 - e \times E_{fb} + E_a \tag{9}$$

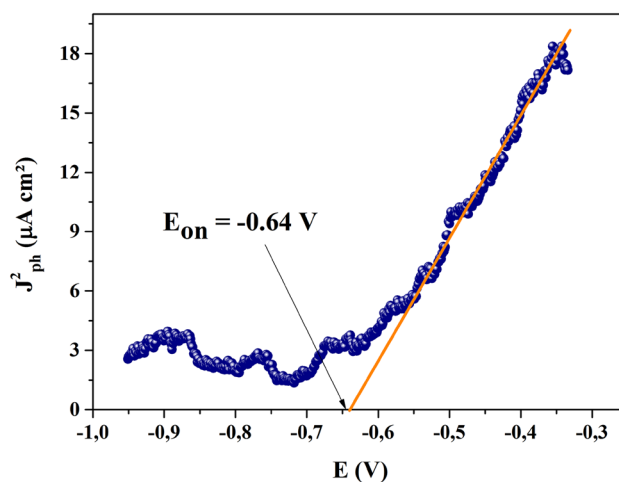


Fig. 8 J-E characteristic of  $SnS_2$  plotted in  $Na_2SO_4$  (0.1 M) electrolyte at a scan rate of  $10 mV s^{-1}$

The  $E_{BC}$  value (−4.02 eV) corresponds to a potential −0.73 V and consists mainly of the  $Sn^{4+} - 5p$  orbital. Therefore, the level of the valence band (VB) located at −6.28 eV (1.53 V) is simply deduced from the relation ( $E_{BV} = E_{BC} - E_g$ ) and is made up of  $S^{2-} - 3p$  orbital with a small admixture of  $Sn^{4+} - 5s$  character. The energy diagram of the junction (Fig. 9) clearly shows the reduction of dissolved oxygen to  $O_2^{\bullet -}$ ; the potential of the couple  $O_2/O_2^{\bullet -}$  (−0.57 V) is taken from ref [38].

The EIS measurement is conducted at free potential, after its stabilization, in neutral medium to quantify the contributions of the electrolyte, bulk and grain boundaries. The EIS diagram of the junction  $SnS_2/Na_2SO_4$  (Fig. 10) reveals two semicircles whose centers are localized below the real axis, indicating that the charge transfer occurs via two successive

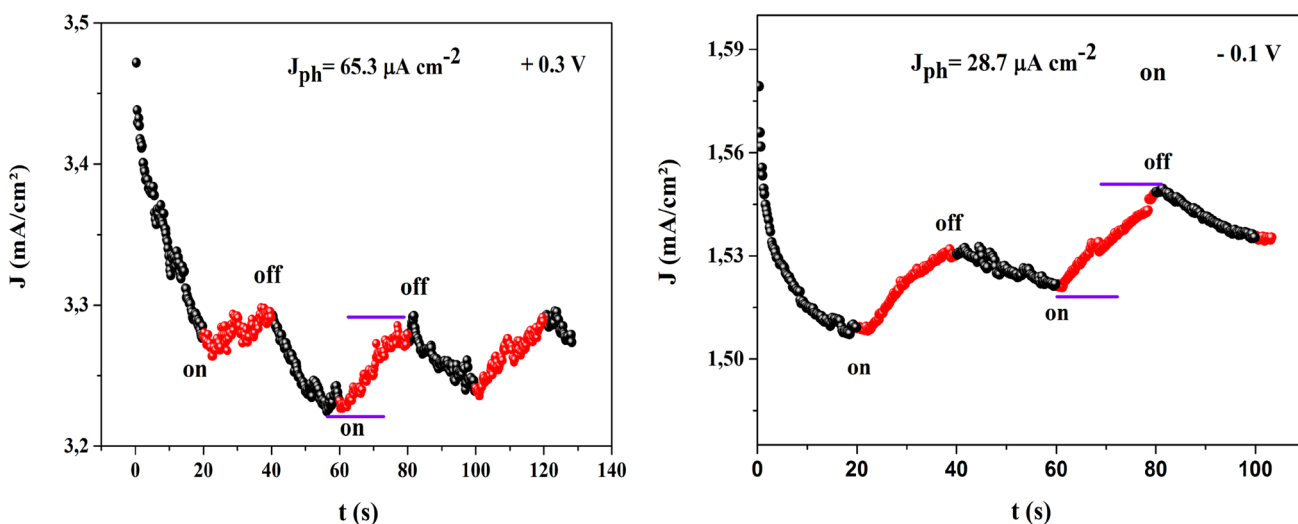
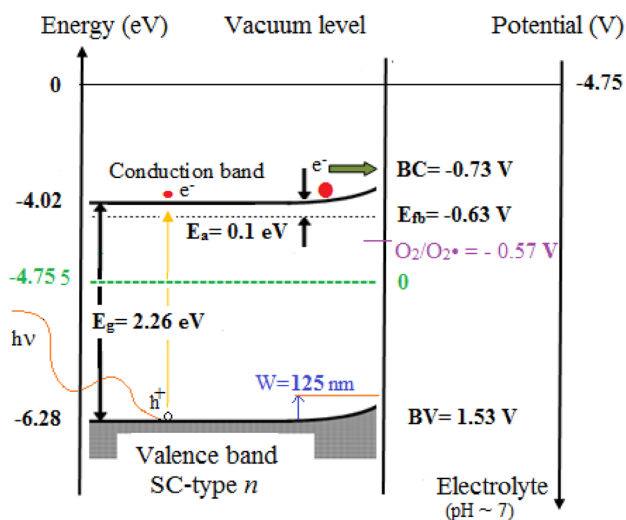
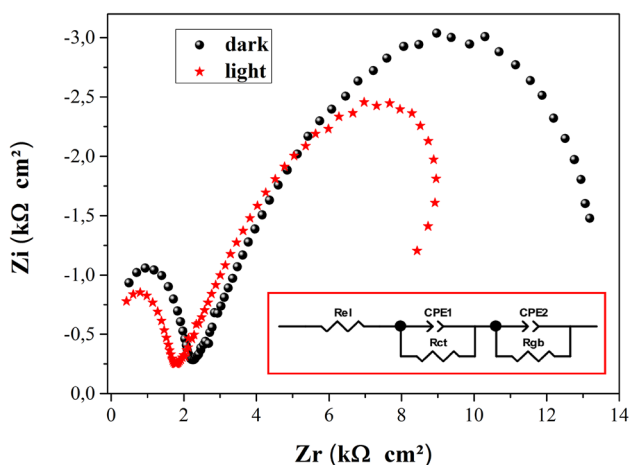


Fig. 7 Photocurrents versus time at different polarizations under chopped light



**Fig. 9** Energy band diagram of the junction  $\text{SnS}_2/\text{Na}_2\text{SO}_4$  electrolyte



**Fig. 10** Nyquist plots of  $\text{SnS}_2$  in  $\text{Na}_2\text{SO}_4$  (0.1 M) in the dark and illumination. Inset: the equivalent electrical circuit

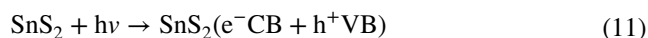
steps. Recent theories suggest the substitution of the capacitance by a constant phase element (CPE), which indicates a deviation from a pure capacitive behavior. In such a case the impedance is defined as follows:

$$Z_{\text{CPE}} = 1/[C(j\omega)^n] \quad (10)$$

$j$  is the imaginary number ( $j^2 = -1$ ); the exponent  $n$  ( $0 < n < 1$ ) is due to the non-uniformity of the field lines, the roughness of the electrode and the presence of surface states in

the gap region. The high frequencies semicircle is assigned to a faradic charge transfer ( $R_{\text{ct}} = 2.46 \text{ k}\Omega \text{ cm}^2$ ) while the second one is due to grain boundaries contribution ( $R_{\text{gb}} = 13.69 \text{ k}\Omega \text{ cm}^2$ ). The offset from the origin corresponds to the electrolytic resistance ( $R_{\text{el}} = -317 \Omega \text{ cm}^2$ ,  $\text{Na}_2\text{SO}_4$  0.1 M). Table 1 summarizes the electrochemical parameters obtained by fitting the EIS spectrum and the data are modeled to an equivalent electrical circuit using the Zview software (Fig. 10, inset).

The photocatalysis is an attractive and low cost alternative for the degradation of hazardous organic compounds [39]. It is based on the activation of  $\text{SnS}_2$  with energetic photons, forming pairs ( $e^-_{\text{CB}}, h^+_{\text{VB}}$ ) that results in excitation of electrons from VB to CB (Eq. 11). The pairs ( $e^-_{\text{CB}}, h^+_{\text{VB}}$ ) react with oxygen and water to generate radicals, which attack the organic matter in solution. The purpose of this reaction is to mineralize the compound into  $\text{CO}_2$  and water.



As application, RhB is successfully oxidized on  $\text{SnS}_2$  powder under solar light. The  $\text{SnS}_2$  surface ( $\text{pzzp} = 1.99$ ) is positively charged and interact electrostatically with RhB through the negatively functional group. The mixture  $\text{SnS}_2/\text{RhB}$  solution ( $10 \text{ mg L}^{-1}$ ) was maintained for 2 h in the dark to reach the adsorption equilibrium; it was then exposed to sunlight. The UV–Vis spectra of the solutions: initial, adsorbed and irradiated solutions are shown in Fig. 11. RhB is a recalcitrant dye and no change in the RhB concentration is observed by photolysis. By contrast 93.67% is removed by adsorption/photocatalysis after 3 h of illumination on  $\text{SnS}_2$ . Table 2 compares our results with previous works [40–44].

## 4 Conclusions

In this present work, the physical properties (structural, optical and photo-electrochemical) and the photoactivity of  $\text{SnS}_2$  prepared by precipitation are studied. The presence of single  $\text{SnS}_2$  phase was confirmed by X-ray diffraction and Raman spectroscopy. Optical energy band gap ( $E_g$ ) value is estimated at 2.26 eV which is close to that required for terrestrial applications and makes  $\text{SnS}_2$  a promising compound for the solar energy conversion.  $\text{SnS}_2$  exhibit  $n$ -type conductivity. The valence and conduction bands of  $\text{SnS}_2$  are determined relatively from the capacitance measurements. The photodegradation ability of Rhodamine B in the presence of  $\text{SnS}_2$  under sunlight is examined. Without catalyst (photolysis) RhB not substantially degrades, but its concentration is reduced by exposition to solar irradiation for 3 h in the presence of  $\text{SnS}_2$

**Table 1** Electrochemical parameters extracted by fitting the EIS data

$\text{SnS}_2$	$R_{\text{s1}} (\Omega \text{ cm}^2)$	CPE 1 (nF/cm <sup>2</sup> )	$n_1$	$R_{\text{ct}} (\text{k}\Omega \text{ cm}^2)$	CPE 2 (μF/cm <sup>2</sup> )	$n_2$	$R_{\text{gb}} (\text{k}\Omega \text{ cm}^2)$
Dark	-316.9	9.73	0.87	2.46	67.42	0.51	13.69
Light	-316.9	9.73	0.87	1.99	84.08	0.47	12.55

**Fig. 11** UV–Vis spectra of photo catalytic degradation of RhB solution under solar light

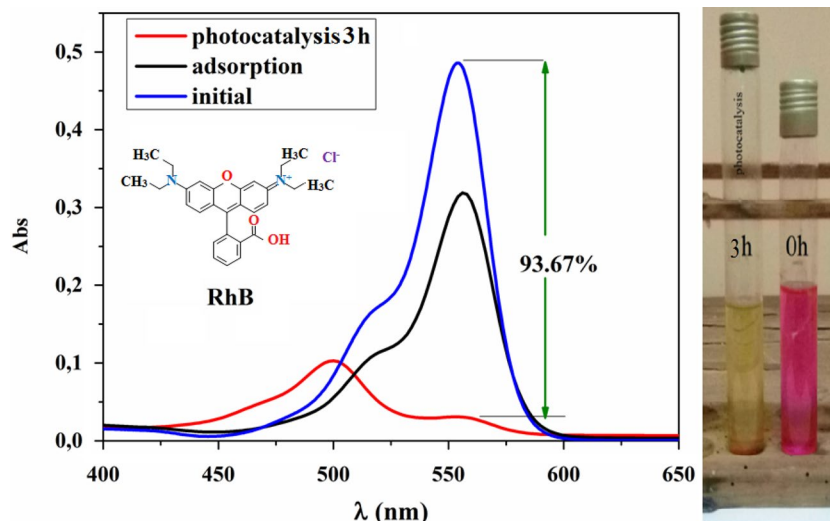


**Table 2** Comparison of results obtained with the literature

SnS <sub>2</sub>	By chemical route	Other method	Ref
E <sub>g</sub> (eV)	2.26	2.7–3	PECVD [37]
Size (nm)	60	20–50	Hydrothermal [38]
RhB%	93.67 (3 h)	90 (8 h)	Hydrothermal [39]
N <sub>D</sub> (cm <sup>-3</sup> )	3.54 × 10 <sup>16</sup>	2.6 × 10 <sup>15</sup>	VTM [40]
J <sub>ph</sub> (mA/cm <sup>2</sup> )	0.07	5	Chemical route [41]

(93.67% degradation). Accordingly, our results showed the potential application of SnS<sub>2</sub> in the visible-light photocatalysts and optoelectronic nanodevices.

**Acknowledgements** This work was supported by the Faculty of Chemistry (U.S.T.H.B., Algiers) with the collaboration of the institute of Molecules & Materials of Le Mans, CNRS, University of Maine, France. The authors would like to thank Pr. A. Azaze for the XRD patterns and Dr. S. Kaizra for his help.

## References

- G. Kiruthigaa, C. Manoharan, C. Raju, S. Dhanapandian, V. Thanikachalam, *Mater. Sci. Semicond. Process.* **26**, 533–539 (2014)
- N.G. Deshpande, A.A. Sagade, Y.G. Gudage, C.D. Lokhande, R. Sharma, *J. Alloys Compd.* **436**, 421–426 (2007)
- A.S. Alqarni, O. A. Yassin, *Mater. Sci. Semicond. Process.* **42**, 390–396 (2016)
- L. Deng, Z. Zhu, L. Liu, H. Liu, *Solid State Sci.* **63**, 76–83 (2017)
- M. Messaoudia, M.S. Aida, N. Attaf, T. Bezzi, J. Bougdira, G. Medjahdi, *Mater. Sci. Semicond. Process.* **17**, 38–42 (2014)
- Y. Liu, Y. Zhang, D. Wu, D. Fan, X. Pang, Y. Zhang, H. Ma, X. Sun, Q. Wei, *Biosens. Bioelectron.* **86**, 301–307 (2016)
- Z. Yang, Y. Ren, Y. Zhang, J. Li, H. Li, X.H.X. Hu, Q. Xu, *Biosens. Bioelectron.* **26**, 4337–4341 (2011)
- Y. Liu, G. Qiu, D. Kong, B. Hu, Y. Li, J. Su, C. Xia, *Superlattices Microstruct.* **111**, 480–486 (2017)
- H. Wu, L. Zhou, S. Yan, H. Song, Y. Shi, *Opt. Commun.* **406**, 239–243 (2018)
- F. Beshkar, S. Zinatloo-Ajabshir, S. Bagheri, M. S. Niasari, *PLoS ONE* **12**(6), e0158549 (2017)
- S. Zinatloo-Ajabshir, S. Mortazavi-Derazkola, M. Salavati-Niasari, *Int. J. Hydrogen Energy* **42**(22), 1–11 (2017)
- S. Zinatloo-Ajabshir, M. Salavati-Niasari, *J. Mol. Liq.* (2017). <https://doi.org/10.1016/j.molliq.2017.08.050>
- F. Razi, S. Zinatloo-Ajabshir, M. Salavati-Niasari, *J. Mol. Liq.* **222**, 435–440 (2016)
- A.S. Alqarni, B.O. Alsobhi, A.A. Elabbar, O. A. Yassin, *Mater. Sci. Semicond. Process.* **59**, 18–22 (2017)
- D. Guan, J. Li, X. Gao, Y. Xie, C. Yuan, *J. Alloys Compd.* **658**, 190–197 (2016)
- I.B. Kherkhachi, A. Attaf, H. Saidi, A. bouhdjar, H. Bendjiddi, Y. Benkhetta, R. Azizi, M. S. Aida, *J. Light Electron. Opt.* **127**, 2266–2270 (2016)
- P.C. Huang, H.I. Wang, S. Brahma, S.C. Wang, J.L. Huang, *J. Cryst. Growth* **468**, 162–168 (2016)
- K. Li, S. Yan, Z. Lin, X. Dai, P. Qu, *Synth. Met.* **217**, 138–143 (2016)
- J. Zai, X. Qian, K. Wang, C. Yu, L. Tao, Y. Xiao, J. Chen, *Cryst. EngComm* **14**, 1364–1375 (2012)
- S.K. Panda, A. Antonakos, E. Liarokapis, S. Bhattacharya, S. Chaudhuri, *Mater. Res. Bull.* **42**, 576–583 (2007)
- L. Chen, M. Chen, D. Jiang, J. Xie, *J. Mol. Catal. A* **425**, 174–182 (2016)
- G. Zhang, X. Du, Y. Wang, H. Wang, W. Wang, Z. Fu, *Mater. Sci. Semicond. Process.* **64**, 77–84 (2017)
- X. Gao, G. Huang, H. Gao, C. Pan, H. Wang, J. Yan, Y. Liu, H. Qiu, N. Ma, J. Gao, *J. Alloys Compd.* **674**, 98–108 (2016)
- H. Tang, X. Qi, W. Han, L. Ren, Y. Liu, X. Wang, *J. Zhong. Appl. Surf. Sci.* **355**, 7–13 (2015)
- Y. Li, S.G. Leonardi, A. Bonavita, G. Neri, W. Wlodarski, *Procedia Eng.* **168**, 1102–1105 (2016)
- S. Zinatloo-Ajabshir, M.S. Morassaei, M. Salavati-Niasari, *J. Cleaner Prod.* **198**, 11–18 (2018)
- Y. El Mendili, J.-F. Bardeau, N. Randrianantoandro, A. Gourbil, J.-M. Grenèche, A. Mercier, F. Grasset, *J. Raman Spectrosc.* **42**, 239–242 (2011)
- Y. El Mendili, J.-F. Bardeau, N. Randrianantoandro, F. Grasset, J.-M. Grenèche, *J. Phys. Chem. C* **116**, 23785–23792 (2012)
- D.G. Mead, J. C. Irwin, *Solid State Commun.* **20**, 885–887 (1976)

30. O.A. Yassin, A.A. Abdelaziz, A. Y. Jaber, *Mater. Sci. Semicond. Process.* **38**, 81–86 (2015)
31. X. Zhou, T. Zhou, J. Hu, J. Li, *CrystEngComm* **14**, 5627–5633 (2012)
32. H. G. Hecht, *J. Res. Natl. Bur. Stan. A* **80** (1976) 567–583
33. J. Katie, M.M. Hukovie, I. Sarie, M. Petravie, *J. Electrochem. Soc.* **164**, 383–389 (2017)
34. S. Kabouche, Y. Louafi, B. Bellal, M. Trari, *Appl. Phys. A* **123**, 545–553 (2017)
35. M.A. Butler, D. S. Ginte, *J. Electrochem. Soc.* **125**, 228–232 (1978)
36. W.M. Haynes, *Handbook of Chemistry and Physics*, 95th edn. (CRC Press, Boca Raton, 2014–2015)
37. S. Omeiri, B. Hadjarab, M. Trari, *Thin Solid Films.* **519**, 4277–4281 (2011)
38. S. Park, J. Park, R. Selvaraj, Y. Kim, *J. Ind. Eng. Chem.* **31**, 269–275 (2015)
39. S. Kaizra, Y. Louafi, B. Bellal, M. Trari, G. Rekhila, *Mater. Sci. Semicond. Process.* **30**, 554–560 (2015)
40. L.L. Cheng, M.H. Liu, S.C. Wang, M.X. Wang, G.D. Wang, Q.Y. Zhou, Z. Q. Chen, *Semicond. Sci. Technol.* **28**, 015020–015027 (2013)
41. Y. Liu, H. Kang, L. Jiao, C. Chen, K. Cao, Y. Wang, H. Yuan, *Nanoscale* **7**, 1325–1332 (2015)
42. Z. Zhang, C. Shao, X. Li, Y. Sun, M. Zhang, J. Mu, P. Zhang, Z. Guo, Y. Liu, *Nanoscale* **5**, 606–618 (2013)
43. M.A. Bryushinin, G.B. Dubrovsky, I.A. Sokolov, *Appl. Phys. B* **68**, 871–875 (1999)
44. T. Wang, H. Meng, X. Yu, Y. Liu, H. Chen, Y. Zhu, J. Tang, Y. Tong, Y. Zhang, *RSC Adv.* **5**, 15469–15478 (2015)